

Non-Hermitian birefringent Dirac fermions driven by electromagnetic fields

Kai Liu(刘恺), Wan-Zi Sun(孙万梓), Cheng-Xi Li(李成蹊), and Wu-Ming Liu(刘伍明)
Citation: Chin. Phys. B, 2025, 34 (**7**): 077104. DOI: 10.1088/1674-1056/adcaa1
http://cpb.iphy.ac.cn; http://iopscience.iop.org/cpb

What follows is a list of articles you may be interested in

Classifying extended, localized and critical states in quasiperiodic lattices via unsupervised learning

Bohan Zheng(郑博涵), Siyu Zhu(朱思宇), Xingping Zhou(周兴平), and Tong Liu(刘通)
Chin. Phys. B, 2025, 34 (**1**): 017103. DOI: 10.1088/1674-1056/ad8cb9

Phase induced localization transition

Tong Liu(刘通), Xingbo Wei(魏兴波), and Youguo Wang(王友国)
Chin. Phys. B, 2024, 33 (**10**): 107103. DOI: 10.1088/1674-1056/ad6a0b

Demonstrate chiral spin currents with nontrivial interactions in superconducting quantum circuit

Xiang-Min Yu(喻祥敏), Xiang Deng(邓翔), Jian-Wen Xu(徐建文), Wen Zheng(郑文), Dong Lan(兰栋), Jie Zhao(赵杰), Xinsheng Tan(谭新生), Shao-Xiong Li(李邵雄), and Yang Yu(于扬)
Chin. Phys. B, 2023, 32 (**4**): 047104. DOI: 10.1088/1674-1056/acac17

Mobility edges generated by the non-Hermitian flatband lattice

Tong Liu(刘通) and Shujie Cheng(成书杰)
Chin. Phys. B, 2023, 32 (**2**): 027102. DOI: 10.1088/1674-1056/ac6581

Resistivity minimum emerges in Anderson impurity model modified with Sachdev-Ye-Kitaev interaction

Lan Zhang(张欄), Yin Zhong(钟寅), and Hong-Gang Luo(罗洪刚)
Chin. Phys. B, 2021, 30 (**4**): 047106. DOI: 10.1088/1674-1056/abefcb

---

Non-Hermitian birefringent Dirac fermions driven by electromagnetic fields

Kai Liu(刘恺)[1,2], Wan-Zi Sun(孙万梓)[1,2], Cheng-Xi Li(李成蹊)[1,2,†], and Wu-Ming Liu(刘伍明)[1,2,3,‡]

[1] *Beijing National Laboratory for Condensed Matter Physics, and Institute of Physics, Chinese Academy of Sciences, Beijing* 100190, *China*
[2] *School of Physical Sciences, University of Chinese Academy of Sciences, Beijing* 100190, *China*
[3] *Songshan Lake Materials Laboratory, Dongguan* 523808, *China*

(Received 17 February 2025; revised manuscript received 8 April 2025; accepted manuscript online 9 April 2025)

We investigate the behavior of non-Hermitian birefringent Dirac fermions by examining their interaction with electromagnetic fields through renormalization group analysis. Our research reveals that the interplay between non-Hermiticity and birefringence leads to distinct behaviors in two and three dimensions, where the system exhibits different fixed points and scaling properties due to dimension-dependent charge renormalization effects. In two dimensions, where the electronic charge remains unrenormalized, the system flows in the deep infrared limit from non-Hermitian birefringent spin-3/2 fermions to two copies of non-Hermitian spin-1/2 Dirac fermions, demonstrating a crossover of relativistic liquid and non-relativistic liquid. In three dimensions, dynamic screening of electromagnetic interactions modifies the logarithmic growth of Fermi velocity, leading to richer quantum corrections while maintaining similar suppression of birefringence in the infrared limit. Our findings provide theoretical insights into the emergence of Lorentz symmetry in non-Hermitian systems, laying theoretical foundations for studying low-energy behavior in other non-Hermitian models.

Keywords: non-Hermitian birefringent Dirac fermions, renormalization group analysis, dimension-dependent charge renormalization, non-Hermitian Fermi velocity, Lorentz symmetry

PACS: 71.10.Fd, 71.10.–w, 71.10.Ay, 71.15.Rf

DOI: 10.1088/1674-1056/adcaa1 **CSTR:** 32038.14.CPB.adcaa1

1. Introduction

Recent advances in non-Hermitian physics and quantum low-energy behavior have become one of the most intriguing research frontiers in condensed matter physics. While traditional quantum systems are described by Hermitian Hamiltonians, non-Hermitian systems with real energy spectra have garnered significant attention for their unique physical properties and potential applications.[1–8] The rich topological structure of these systems has been extensively explored,[9,10] with recent studies revealing profound connections between non-Hermiticity and quantum criticality.[11] Meanwhile, the experimental realization of birefringent Dirac materials, which exhibit two distinct Fermi velocities in their low-energy excitations, has provided a novel platform for investigating quantum low-energy behavior.[12–16]

However, many fundamental questions remain regarding the low-energy behavior of non-Hermitian birefringent systems when coupled to electromagnetic fields.[8,17–20] In particular, the conventional understanding of quantum systems becomes inadequate when both non-Hermiticity and birefringence are present.[21–23] Key questions emerge: How does the interplay between non-Hermiticity and birefringence affect the system's low-energy behavior? Do new symmetries emerge in the infrared limit?[24] How do the non-Hermitian parameter, birefringent parameter, and Fermi velocities evolve under renormalization group flow?[25–27] These questions are not only crucial for understanding the universality of quantum field theory but also have profound implications for the emergence of non-Hermitian relativistic fermions in condensed matter systems.[28–30]

In this paper, we systematically investigate the quantum electrodynamics of non-Hermitian birefringent Dirac fermions through renormalization group analysis. By deriving and solving coupled differential equations that characterize the system's scaling behavior, we track the evolution of system parameters across different energy scales in both two and three dimensions. Our analysis reveals distinct behaviors arising from dimension-dependent charge renormalization effects: in two dimensions, where the electronic charge remains unrenormalized, the system flows in the deep infrared limit from non-Hermitian birefringent spin-3/2 fermions to two copies of non-Hermitian spin-1/2 Dirac fermions; in three dimensions, dynamic screening of electromagnetic interactions leads to richer quantum corrections while maintaining similar suppression of birefringence in the infrared limit.

We demonstrate that under renormalization group flow, despite the explicit breaking of Hermiticity and Lorentz invariance at the microscopic level, the system exhibits universal be-

†Corresponding author. E-mail: lcxtom@icloud.com
‡Corresponding author. E-mail: wliu@iphy.ac.cn

© 2025 Chinese Physical Society and IOP Publishing Ltd. All rights, including for text and data mining, AI training, and similar technologies, are reserved.

havior in the low-energy limit. At the infrared fixed point, the birefringent parameter asymptotically approaches zero while maintaining real energy spectra, suggesting the natural emergence of non-Hermitian Lorentz symmetry. These findings not only deepen our understanding of non-Hermitian quantum criticality but also provide new perspectives on the fundamental role of non-Hermitian relativistic fermions in quantum field theory.

Recent experimental advances have made significant progress in realizing non-Hermitian quantum systems.[6,33] Notably, Yu *et al.*[34] have demonstrated a groundbreaking approach for constructing non-Hermitian models through open systems with controlled dissipation. In their work published in Physical Review Letters, they clearly articulated how open quantum systems can be engineered to exhibit effective non-Hermitian Hamiltonians with precisely controlled parameters. Their experimental framework provides a promising route for implementing the non-Hermitian birefringent Dirac systems we investigate in this study, establishing a crucial bridge between our theoretical predictions and potential experimental realizations. These experimental techniques enable the direct observation of non-Hermitian effects, including asymmetric transport phenomena and exceptional point physics, which are central to verifying the renormalization group behavior we predict.

2. Model and method

We consider a non-Hermitian birefringent Dirac system described by the Hamiltonian[26]

$$H_{\mathrm{BF,NH}}(\boldsymbol{k}) = H_{\mathrm{BF}}(\boldsymbol{k}) + \alpha M H_{\mathrm{BF}}(\boldsymbol{k}), \tag{1}$$

where $H_{\mathrm{BF}}(\boldsymbol{k})$ is the Hermitian birefringent Dirac Hamiltonian, α characterizes the strength of non-Hermiticity, and M is a Hermitian operator satisfying $M^2 = 1$ and $\{M, H_{\mathrm{BF}}\} = 0$, where $\{A,B\} = AB + BA$ denotes the anticommutator. As illustrated in Fig. 1, this system can be realized in a lattice model with asymmetric hopping amplitudes that gives rise to non-Hermitian birefringent Dirac cones. Therefore, $(\alpha M H_{\mathrm{BF}})^\dagger = \alpha H_{\mathrm{BF}}^\dagger M^\dagger = \alpha H_{\mathrm{BF}} M = -\alpha M H_{\mathrm{BF}}$, which demonstrates that the term $\alpha M H_{\mathrm{BF}}(\boldsymbol{k})$ is anti-Hermitian. This structure makes the total Hamiltonian $H_{\mathrm{BF,NH}}(\boldsymbol{k})$ a combination of Hermitian and anti-Hermitian components, giving rise to its non-Hermitian character. The eigenvalues of this operator are $\pm E^{\pm}_{\mathrm{NH}}(\boldsymbol{k})$, where $E^{\pm}_{\mathrm{NH}}(\boldsymbol{k}) = (1 \pm \beta) v_{\mathrm{F}} |\boldsymbol{k}|$ with $v_{\mathrm{F}} = \sqrt{v_{\mathrm{H}}^2 - v_{\mathrm{NH}}^2}$ and $v_{\mathrm{NH}} = \alpha v_{\mathrm{H}}$. The system exhibits real energy spectra when $|\alpha| < 1$.[35–37]

The Hermitian birefringent Hamiltonian $H_{\mathrm{BF}}(\boldsymbol{k})$ takes the form $H_{\mathrm{BF}}(\boldsymbol{k}) = v_{\mathrm{H}} H_1(\boldsymbol{k}) + \beta v_{\mathrm{H}} H_2(\boldsymbol{k})$, which is constructed from two mutually commuting Dirac operators $H_1(\boldsymbol{k}) = \sum_{j=1}^{d} \Gamma_{j0} k_j$ and $H_2(\boldsymbol{k}) = \sum_{j=1}^{d} \Gamma_{0j} k_j$. The gamma matrices $\Gamma_{j0} = \sigma_j \otimes \tau_0$ and $\Gamma_{0j} = \sigma_0 \otimes \tau_j$ are constructed from Pauli matrices satisfying the Clifford algebra $\{\Gamma_{j0}, \Gamma_{k0}\} = 2\delta_{jk}$, $\{\Gamma_{0j}, \Gamma_{0k}\} = 2\delta_{jk}$, $[\Gamma_{j0}, \Gamma_{0k}] = 0$, while v_{H} represents the Fermi velocity and β denotes a dimensionless parameter characterizing the strength of birefringence. In the three-dimensional (3D) case ($d = 3$), these gamma matrices take the form $\eta \otimes \Gamma_{j0}$ and $\eta \otimes \Gamma_{0j}$ respectively, with $\eta = \mathrm{diag}(1, -1)$.

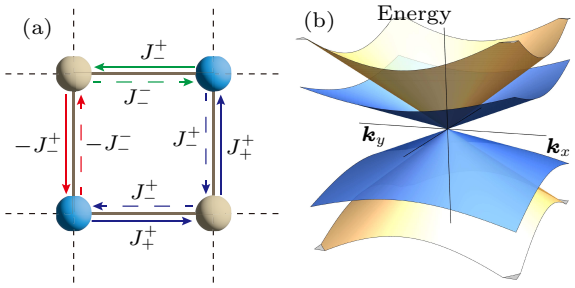


Fig. 1. (a) Schematic representation of non-Hermitian birefringent Dirac systems in two dimensions. A four-site unit-cell of a generalized π-flux square lattice. The system exhibits two distinct hopping amplitudes characterized by $J_\pm = J_0(1 \pm \beta)$, where J_0 represents the average hopping strength and β is the dimensionless birefringent parameter. The nearest-neighbor hopping amplitudes, indicated by directional arrows, give rise to gapless non-Hermitian birefringent Dirac fermions. Here, $j_\pm^+ = j_+(1 \pm \alpha)$ and $j_\pm^- = j_-(1 \pm \alpha)$, where the dimensionless parameter α quantifies the non-Hermiticity strength, resulting in asymmetric hopping amplitudes between adjacent sites in opposite directions. (b) For the Dirac cones under birefringence, the dispersion relation is given by $E^{\pm}_{\mathrm{NH}}(\boldsymbol{k}) = (1 \pm \beta) v_{\mathrm{F}} |\boldsymbol{k}|$, where $v_{\mathrm{F}} = \sqrt{v_{\mathrm{H}}^2 - v_{\mathrm{NH}}^2}$ and $v_{\mathrm{NH}} = \alpha v_{\mathrm{H}}$.

The interaction between this system and electromagnetic fields is described by the quantum electrodynamics action

$$\begin{aligned} S_{\mathrm{QED}} &= \int \mathrm{d}\tau d^D \boldsymbol{x}\ (L_{\mathrm{F}} + L_{\mathrm{EM}}), \\ L_{\mathrm{F}} &= \Psi^\dagger \left[\partial_\tau - \mathrm{i} e A_0 + H_{\mathrm{BF,NH}} \left(\boldsymbol{k} \to -\mathrm{i}\boldsymbol{\nabla} - \frac{e}{c} \boldsymbol{A} \right) \right] \Psi, \\ L_{\mathrm{EM}} &= \frac{1}{4} F_{\mu\nu} F_{\mu\nu} + \frac{1}{2\xi} (\partial_\mu A_\mu)^2, \end{aligned} \tag{2}$$

where e is the electronic charge, L_{F} represents the fermionic Lagrangian, L_{EM} denotes the Maxwell Lagrangian, and $F_{\mu\nu} = \partial_\mu A_\nu - \partial_\nu A_\mu$ is the electromagnetic field strength tensor.

The dynamics of the system is determined by the fermionic Green's function, which captures both the non-Hermitian nature and birefringent properties of the system:

$$\begin{aligned} S(k) = & \frac{-\mathrm{i}\omega + H_{\mathrm{BF,NH}}(\boldsymbol{k})}{\omega^2 + (1+\beta)^2 v_{\mathrm{F}}^2 |\boldsymbol{k}|^2} \\ & \times \frac{\omega^2 + (1+\beta^2) v_{\mathrm{F}}^2 |\boldsymbol{k}|^2 - 2\beta v_{\mathrm{F}}^2 H_1(\boldsymbol{k}) H_2(\boldsymbol{k})}{\omega^2 + (1-\beta)^2 v_{\mathrm{F}}^2 |\boldsymbol{k}|^2}. \end{aligned} \tag{3}$$

To fully characterize the electromagnetic interactions in our system, we need to consider the gauge field propagator. In the case of $3+1$ dimensions, the propagator takes a relatively simple form that accounts for both temporal and spatial components: $D_{\mu\nu}(k) = \delta_{\mu\nu} / (\varepsilon[\omega^2/c^2 + |\boldsymbol{k}|^2])$. Here, the electromagnetic properties of the medium play a crucial role, with the speed of light in the medium given by $c = c_0/\sqrt{\varepsilon\mu}$, where ε and μ represent the medium's permittivity and permeability respectively. The frequency component ω appears as the

Matsubara frequency in our formalism, reflecting the quantum nature of the electromagnetic interactions.

In $d=2$ dimensions, the non-analytic structure of the gauge field propagator can be derived by integrating the three-dimensional analytic propagator over the momentum in the z direction (k_z), yielding a more compact form: $\tilde{D}_{\mu\nu}(k) = \delta_{\mu\nu}/(2\varepsilon\sqrt{\omega^2/c^2+|\boldsymbol{k}_\perp|^2})$, where $\boldsymbol{k}_\perp=(k_x,k_y)$ represents the in-plane momentum components.

The speed of light does not renormalize in $d=2$, while it receives perturbative corrections due to many-body dynamic screening in $d=3$. These outcomes directly follow from the fact that the polarization bubble in $d=3$ and $d=2$ are respectively logarithmically divergent and finite.

The quantum corrections to our non-Hermitian birefringent system arise from the interaction between Dirac fermions and electromagnetic fields. To properly account for these interactions in our theoretical framework, we need to carefully examine the coupling between the fermionic and electromagnetic fields. The interaction vertex between NH birefringent Dirac fermions and photons is given by $e\gamma_\mu$, where $\mu=0,j;\ j=1,\ldots,d$. For the non-Hermitian case, the gamma matrices take a modified form that incorporates both the non-Hermitian and birefringent nature of our system: $\gamma_0=i$ and $\gamma_j=\frac{v_{\rm H}}{c}(1+\alpha M)(\Gamma_{j0}+\beta\Gamma_{0j})$. This structure reflects how the non-Hermiticity parameter α and the birefringence parameter β jointly influence the electromagnetic coupling of the system.

3. Relativistic RG analysis in two dimensions

The quantum corrections to our non-Hermitian birefringent system can be systematically analyzed using dimensional regularization in $d=2-\varepsilon$ dimensions.[38,39] Following standard quantum field theory methods while carefully accounting for the non-Hermitian nature of our system, we perform extensive algebraic manipulations to evaluate the quantum corrections (see Appendix A). The one-loop fermion self-energy is given by $\Sigma_{1\,\rm loop}(p)$.

Based on these quantum corrections, we can derive the renormalization group (RG) flow equations for the velocity parameters in $d=2$ dimensions. These equations capture how the system's parameters evolve under scaling transformations, with the corrections arising from the quantum electrodynamics (QED) interactions between non-Hermitian birefringent Dirac fermions and electromagnetic fields. The RG flow equations are given by the following expressions:

$$\begin{aligned}\frac{{\rm d}v_{\rm H}}{{\rm d}l} &= v_{\rm H}\{\left[1-2(1+\beta^2)v_{\rm F}^2\right]F_1(v_{\rm F},\beta)\\ &\quad+\left[1+2(1-\beta^2)v_{\rm F}^2-4(1+\beta^4)v_{\rm F}^4\right]F_2(v_{\rm F},\beta)\\ &\quad+4(1-\beta^2)v_{\rm F}^2F_3(v_{\rm F},\beta)\},\\ \frac{{\rm d}\beta}{{\rm d}l} &= -4\beta(1-\beta^2)v_{\rm F}^2F_2(v_{\rm F},\beta)\\ &\quad-8\beta(1-\beta^2)v_{\rm F}^2F_3(v_{\rm F},\beta),\end{aligned}\tag{4}$$

where we have used natural units ($c=1$) and $F_1(v_{\rm F},\beta)$, $F_2(v_{\rm F},\beta)$, and $F_3(v_{\rm F},\beta)$ are dimensionless functions defined in Appendix A, along with the auxiliary function $f(x,y)$. These equations reveal that under RG flow, the system approaches a fixed point where $v_{\rm F}\to c$ and $\beta\to 0$, indicating the emergence of non-Hermitian Lorentz symmetry and non-Hermitian pseudo spin-1/2 Dirac fermions in the infrared limit.

The renormalization group equations (4) yield numerical solutions that reveal rich dynamical behavior. To better understand the physical implications of these equations and visualize the system's evolution under RG flow, we perform detailed numerical analysis using representative initial conditions. We investigate the RG flow by examining four representative sets of initial parameters (v_0,β_0,α): $(0.2,0.5,0.2)$, $(0.2,0.5,0.5)$, $(0.8,0.7,0.8)$, and $(0.5,0.9,0.5)$ (Fig. 2). As the RG scale parameter l increases, a remarkable universal pattern emerges: both the Hermitian velocity $v_{\rm H}$ and non-Hermitian velocity $v_{\rm NH}$ exhibit monotonic growth and can exceed the speed of light, while their squared difference — the average effective Fermi velocity $v_{\rm F}$ — consistently approaches but never exceeds the speed of light, independent of initial conditions, highlighting the robustness and universality of this fixed point.

This universal behavior demonstrates the emergence of non-Hermitian Lorentz symmetry under RG flow, representing a fundamental organizing principle in the low-energy physics.[37] Simultaneously, we observed that both the birefringence parameter β and the velocity difference $\beta v_{\rm F}$ decay monotonically to zero with increasing RG scale parameter. This flow pattern indicates a profound transformation in the infrared limit: the non-Hermitian birefringent pseudospin-$3/2$ Dirac fermions evolve into two degenerate non-Hermitian pseudospin-$1/2$ Dirac fermions. For the parameter regime $0<\beta<1$, the Hamiltonian $H(k)$ exhibits a four-dimensional (4D) minimal irreducible representation, constituting a pseudospin-$3/2$ system with four distinct eigenvalue branches; whereas when $\beta=0$, the system undergoes degeneracy, reducing to a doubly degenerate two-level system that precisely corresponds to standard pseudospin-$1/2$ Dirac fermions. This remarkable feature provides compelling evidence for the natural emergence of non-Hermitian spin-$1/2$ fermions in low-energy effective theories.

The non-Hermitian birefringent fermionic propagator exhibits anomalous scaling dimension at the infrared fixed point

$$\begin{aligned}S(k)&\sim S_0(k)\left(\frac{\mu}{k}\right)^{-e^2/12\pi^2\varepsilon},\\ S(\rho k)&=\rho^{-1+e^2/12\pi^2\varepsilon}S(k),\end{aligned}\tag{6}$$

where $S_0(k)$ is the free non-Hermitian fermion propagator and ρ is the scaling transformation coefficient.

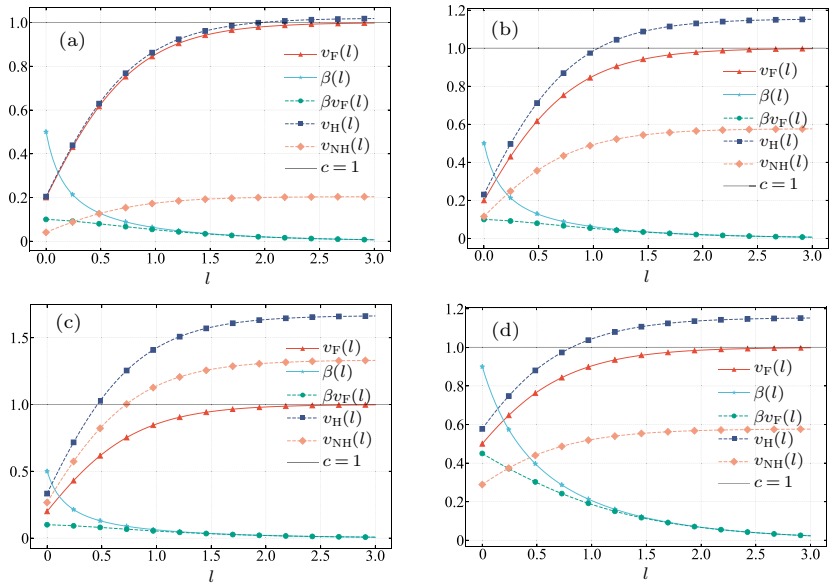


Fig. 2. Renormalization group (RG) flow of the average effective Fermi velocity ($v_{\rm F}$), birefringence parameter (β), and their product $\beta v_{\rm F}$ for quasirelativistic pseudospin-3/2 fermions in the presence of full electromagnetic interactions in two dimensions, where $v_{\rm H}$ represents the velocity of birefringent fermions in Hermitian system and $v_{\rm NH}$ represents the velocity in non-Hermitian system. Initial conditions are: (a) $v_0 = 0.2$, $\beta_0 = 0.5$, $\alpha = 0.2$; (b) $v_0 = 0.2$, $\beta_0 = 0.5$, $\alpha = 0.5$; (c) $v_0 = 0.8$, $\beta_0 = 0.7$, $\alpha = 0.8$; (d) $v_0 = 0.5$, $\beta_0 = 0.9$, $\alpha = 0.5$. As the RG time $l = 3e^2\ln(\Lambda/\kappa)/16\pi^2\varepsilon$ increases, the average effective Fermi velocity $v_{\rm F}$ approaches the speed of light c, while both the birefringence parameter and the birefringence-induced Fermi velocity difference $\beta v_{\rm F}$ asymptotically approach zero. All variables shown are dimensionless, as we set $c = 1$.

In the vicinity of the fixed point, non-Hermitian birefringent Dirac materials exhibit characteristics markedly distinct from those of traditional Fermi liquids and conventional Hermitian systems. The non-Hermitian birefringent Dirac field acquires an anomalous dimension, indicating behavior that diverges from classical expectations in both Hermitian and non-Hermitian contexts. This anomalous dimension causes the Green's function to display non-standard scaling behavior under changes of scale, deviating from simple power-law scaling. This phenomenon reflects the intricate interplay between non-Hermiticity and birefringence, leading to novel quantum effects near the quantum critical point.

3.1. Non-relativistic RG analysis in two dimensions

The non-relativistic limit of non-Hermitian birefringent systems presents unique features in quantum corrections that differ significantly from the relativistic case. This regime, characterized by $v_{\rm F} \ll c$, is especially pertinent to experimental realizations in condensed matter physics. The one-loop fermion self-energy is given by $\Sigma_{1\,\rm loop}(p)$ (detailed derivations are provided in the Appendix A).

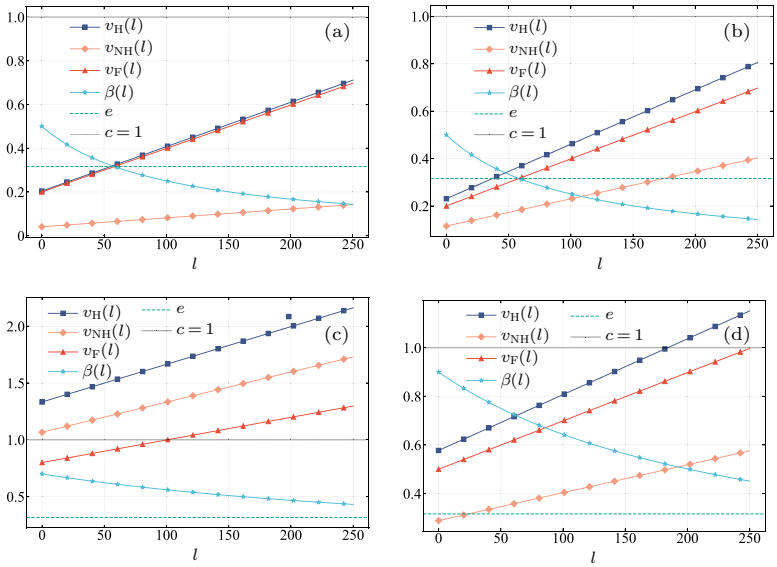


Fig. 3. Renormalization group (RG) flow of the average effective Fermi velocity ($v_{\rm F}$), birefringence parameter (β), and their product $\beta v_{\rm F}$ for quasirelativistic pseudospin-3/2 fermions in the presence of Coulomb interactions in two dimensions, where $v_{\rm H}$ represents the average velocity of birefringent fermions in Hermitian system and $v_{\rm NH}$ represents the average velocity in non-Hermitian system. Initial conditions are (a) $v_0 = 0.2$, $\beta_0 = 0.5$, $\alpha = 0.2$; (b) $v_0 = 0.2$, $\beta_0 = 0.5$, $\alpha = 0.5$; (c) $v_0 = 0.8$, $\beta_0 = 0.7$, $\alpha = 0.8$; (d) $v_0 = 0.5$, $\beta_0 = 0.9$, $\alpha = 0.5$. In the non-relativistic regime where $c \to \infty$, as the RG scale parameter $l = \ln(\Lambda/\kappa)$ increases, the average effective Fermi velocity $v_{\rm F}$ shows logarithmic divergence, while the birefringence parameter β approaches zero. However, their product $\beta v_{\rm F}$ remains marginal under renormalization.

The renormalization group (RG) flow equations for the velocity parameters in $d = 2$ dimensions are derived from the perturbative corrections to the system's parameters. These corrections arise from the quantum electrodynamics (QED) interactions between non-Hermitian birefringent Dirac fermions and electromagnetic fields. The RG flow equations are given by

$$\frac{\mathrm{d}v_{\mathrm{F}}}{\mathrm{d}l} = \frac{e^2}{16\pi},$$
$$\frac{\mathrm{d}\beta}{\mathrm{d}l} = -\frac{e^2\beta}{16\pi v_{\mathrm{F}}}, \tag{7}$$

where we have used natural units ($\varepsilon = 1$) and $v_{\mathrm{H}} = v_{\mathrm{F}}/\sqrt{1-\alpha^2}$ are Herimitian birefringent Dirace velocity.

In two-dimensional (2D) interacting quasi-relativistic spin-3/2 Fermi liquids, we observed logarithmic enhancement of the average effective Fermi velocity (v_{F}) accompanied by logarithmic suppression of the birefringence parameter (β), while their product βv_{F} remains marginal under renormalization (see Fig. 3). In the deep infrared regime, the system effectively decouples into two copies of non-Hermitian spin-1/2 relativistic fermions, as manifested by the hierarchy $v_+ - v_- \ll v$, ($v_\pm = 2J_\pm$), which consequently yields $\beta v_{\mathrm{F}} \ll v$. This emergent state can be characterized as an effective critical Fermi liquid of spin-1/2 fermions.

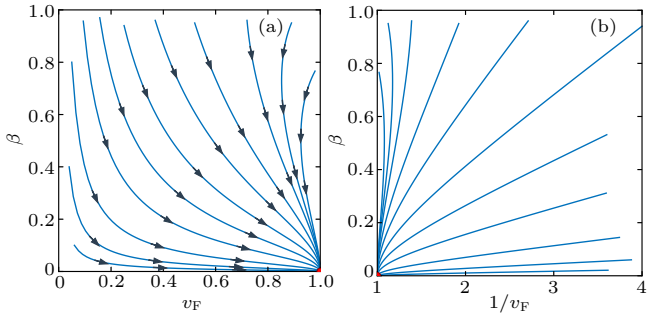


Fig. 4. RG flow of the velocity v and birefringence parameter β for (a) relativistic case and (b) non-relativistic case. In the relativistic regime (a), the flow diagram reveals a stable fixed point at $(v_{\mathrm{F}}, \beta) = (1, 0)$, demonstrating the robustness of emergent Lorentz symmetry. In the non-relativistic regime (b), as $1/v_{\mathrm{F}}$ increases (i.e., v_{F} decreases), the system rapidly returns to the non-relativistic scenario where the product βv_{F} remains constant under renormalization.

Further insight can be gained by numerically solving the coupled renormalization group equations for v_{F} and β, which reveals the distinct flow patterns in both relativistic and non-relativistic regimes. As shown in Fig. 4, the renormalization flow diagram in the non-relativistic limit constitutes a subset of the relativistic case. In the non-relativistic regime, where the average effective Fermi velocity v_{F} is significantly below the speed of light c, βv_{F} remains approximately constant. However, as v_{F} approaches c, βv_{F} begins to decrease, ultimately vanishing when v_{F} reaches c, transforming the spin-3/2 birefringent Dirac fermions into doubly degenerate spin-1/2 Dirac fermions. Notably, in the relativistic regime, the birefringent Dirac field acquires additional anomalous dimensions, driving a crossover of relativistic Fermi liquid to non-relativistic liquid behavior — a phase crossover induced by relativistic effects. Moreover, we find that allowing $\beta > 1$ merely corresponds to an interchange in the roles of v_{F} and βv_{F}, indicating the equivalence of different Dirac matrix representations. Consequently, the two infrared stable fixed points observed in the flow diagram can be regarded as physically identical.[41,42]

3.2. Non-relativistic RG analysis in three dimensions

The 3D non-Hermitian birefringent systems exhibit richer physical phenomena due to the additional spatial dimension.[12,43,44] In the non-relativistic regime where the Fermi velocity is much smaller than the speed of light ($v_{\mathrm{F}} \ll c$), quantum corrections demonstrate distinct features that warrant careful investigation. This regime is particularly relevant for condensed matter realizations of non-Hermitian birefringent materials.

The non-Hermitian birefringent Hamiltonian in three dimensions requires 8×8 matrices and takes the form $H_{\mathrm{BF,NH}}(\boldsymbol{k}) = H_{\mathrm{BF}}(\boldsymbol{k}) + \alpha M H_{\mathrm{BF}}(\boldsymbol{k})$, where $0 < \alpha < 1$, $M^2 = \mathbb{I}_8$, $[M, H_{\mathrm{BF}}(\boldsymbol{k})] = 0$, and $H_{\mathrm{BF}}(\boldsymbol{k})$ is constructed as

$$H_{\mathrm{BF}}(\boldsymbol{k}) = v_{\mathrm{H}} H_1(\boldsymbol{k}) + v_{\mathrm{H}}\beta H_2(\boldsymbol{k}),$$
$$H_1(\boldsymbol{k}) = \Gamma_{310}k_1 + \Gamma_{320}k_2 + \Gamma_{330}k_3,$$
$$H_2(\boldsymbol{k}) = \Gamma_{301}k_1 + \Gamma_{302}k_2 + \Gamma_{303}k_3. \tag{8}$$

The quantum corrections in three dimensions arise from both fermionic and photonic contributions. The one-loop fermion self-energy $\Sigma_{1\,\mathrm{loop}}(p)$ (detailed derivations are provided in the Appendix A) determines the renormalization of the velocity parameters, while the photon self-energy, through screening effects, governs the renormalization of the coupling constant. Evaluating these quantum corrections yields the following RG flow equations[45]

$$\mu\frac{\mathrm{d}v_{\mathrm{F}}}{\mathrm{d}\mu} = -\frac{e^2}{6\pi^2\varepsilon},\ \mu\frac{\mathrm{d}\beta}{\mathrm{d}\mu} = \frac{e^2}{6\pi^2\varepsilon}\frac{\beta}{v_{\mathrm{F}}},\ \mu\frac{\mathrm{d}e}{\mathrm{d}\mu} = \frac{N_f e^3}{6\pi^2 v_{\mathrm{F}}}. \tag{9}$$

These equations reveal that in three dimensions, both the Fermi velocity and the birefringence parameter receive quantum corrections, while the coupling constant undergoes renormalization due to screening effects. The flow of these parameters indicates that the system approaches a fixed point where the birefringence is suppressed. While this behavior shares similarities with the 2D case, the 3D system exhibits richer physics due to the dynamical screening of the electromagnetic interaction, manifested through the running of the coupling constant.

The presence of non-Hermiticity modifies the velocities according to the following expressions:

$$v_{\mathrm{H}} = \frac{1}{\sqrt{1-\alpha^2}}v_{\mathrm{F}},\ v_{\mathrm{NH}} = \frac{\alpha}{\sqrt{1-\alpha^2}}v_{\mathrm{F}}, \tag{10}$$

where v_{F} represents the effective Fermi velocity of the system, v_{H} denotes the average velocity of birefringent fermions in the Hermitian system, and v_{NH} represents the average velocity in the non-Hermitian system. These relations demonstrate how the non-Hermitian parameter α affects the effective velocities in the system.

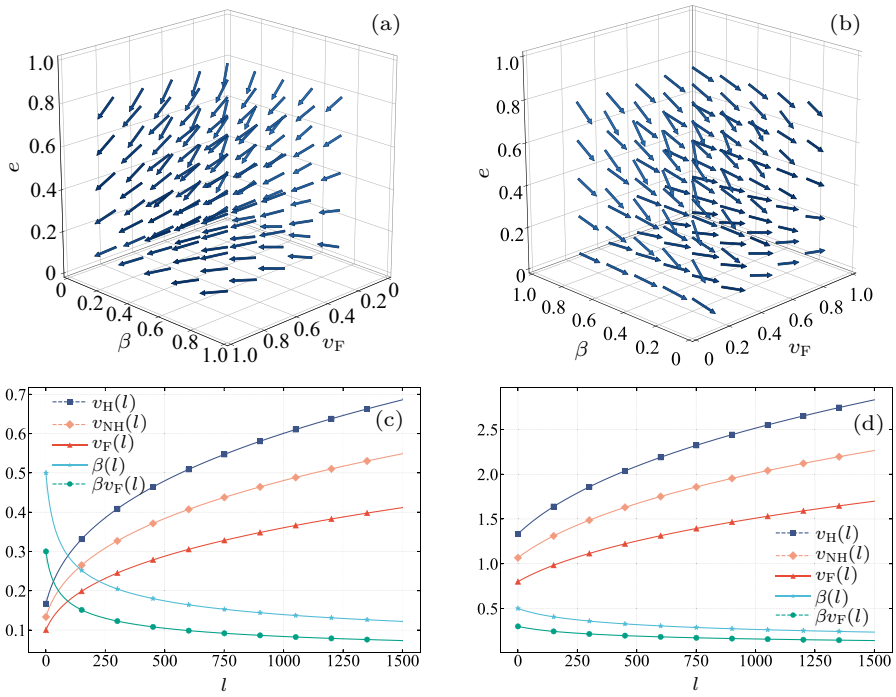


Fig. 5. RG flow of the velocity v and birefringence parameter β under the influence of full electromagnetic interactions for (a) and (b) showing different viewing angles of the flow diagram, where the coupling constant undergoes Coulomb screening and the flow approaches a fixed point at $v_{\mathrm{F}} \to \infty$ in the relativistic regime. Initial conditions for panels (c) and (d) are $v_{\mathrm{F0}} = 0.1$ and 0.8 respectively, with $\beta_0 = 0.5$, $e_0 = 0.3$, $\alpha = 0.8$. As RG time increases, v_{F} shows logarithmic divergence while β approaches zero, with βv_{F} remaining marginal.

The numerical solutions of the RG equations in three dimensions reveal rich dynamical behavior, as shown in Fig. 5. The vector field plots from different viewing angles (panels (a) and (b)) demonstrate how the system flows under renormalization, with the coupling constant experiencing Coulomb screening effects. The flow pattern indicates that the system approaches a fixed point in the relativistic regime where $v_{\mathrm{F}} \to \infty$, suggesting the emergence of relativistic behavior despite starting from non-relativistic initial conditions. Figures 5(c) and 5(d) show the evolution of system parameters for different initial Fermi velocities ($v_{\mathrm{F0}} = 0.1$ and 0.8 respectively). In both cases, we observe that v_{F} exhibits logarithmic divergence while β approaches zero as the RG time increases. Notably, their product βv_{F} remains marginal under renormalization, indicating a preserved scale in the system. This behavior persists regardless of the initial conditions, demonstrating the universality of the RG flow in 3D non-Hermitian birefringent systems. The presence of non-Hermiticity, characterized by $\alpha = 0.8$, modifies the effective velocities but preserves the general structure of the RG flow.

The distinct behaviors of the effective Fermi velocity v_{F} in two and three dimensions reveal fundamental differences in the quantum electrodynamics of non-Hermitian birefringent systems. In both cases, v_{F} exhibits logarithmic growth under renormalization group flow, but the underlying mechanisms differ significantly due to charge renormalization effects. In two dimensions, the coupling constant remains unrenormalized, leading to a straightforward logarithmic enhancement of v_{F}. In contrast, the three-dimensional system experiences dynamic screening of the electromagnetic interaction, manifested through the running of the coupling constant e. This screening effect modifies the logarithmic growth of v_{F} in three dimensions, resulting in a more complex interplay between the velocity renormalization and charge screening. These dimension-dependent behaviors highlight how the quantum corrections to non-Hermitian birefringent systems are fundamentally influenced by the nature of electromagnetic interactions in different spatial dimensions.

4. Conclusions

In this work, we have developed a comprehensive theoretical framework for understanding the quantum electrodynamics of non-Hermitian birefringent Dirac fermions. By introducing an anti-Hermitian term to the conventional birefringent Dirac Hamiltonian while maintaining real energy spectra, we have established a platform for investigating the interplay between non-Hermiticity, birefringence, and electromagnetic interactions.

Our analysis of quantum corrections has revealed rich physical phenomena arising from this interplay. The fermion

self-energy exhibits unconventional behavior due to the presence of both non-Hermiticity and birefringence, while remarkably, the Ward identity remains valid despite the non-Hermitian nature of the system. Furthermore, the polarization bubble shows distinctive features stemming from the presence of two different Fermi velocities, leading to modified electromagnetic responses.

Perhaps most remarkably, our renormalization group analysis demonstrates that the system flows toward a fixed point where Lorentz symmetry emerges in the infrared limit. This unexpected restoration of relativistic invariance, despite the initial presence of non-Hermitian effects and birefringence, suggests that the low-energy physics of our system is governed by principles more fundamental than its microscopic details would suggest. This finding not only deepens our understanding of non-Hermitian quantum field theory but also bridges the gap between non-Hermitian physics and conventional quantum field theory.

The implications of our work extend beyond theoretical interest, pointing toward new possibilities in experimental quantum materials. The framework we have developed provides guidance for realizing and controlling novel quantum states of matter, particularly in systems where non-Hermiticity and birefringence coexist. Future investigations may reveal additional rich phenomena when considering other types of interactions or symmetry-breaking terms, potentially leading to new phases of matter at the intersection of non-Hermitian physics and topological materials.

Appendix A

A1. One-loop fermion self-energy

The one-loop fermion self-energy in our non-Hermitian birefringent system can be calculated using standard quantum field theory techniques. The self-energy is given by

$$\begin{aligned}\Sigma_{1\,\mathrm{loop}}(p) &= e^2\int\frac{\mathrm{d}^3k}{(2\pi)^3}\gamma_\mu S(k)\gamma_\nu\tilde{D}_{\mu\nu}(p-k)\\ &= \frac{e^2}{2\varepsilon}\int\frac{\mathrm{d}^3k}{(2\pi)^3}\gamma_\mu\frac{-\mathrm{i}k_0+H_{\mathrm{BF,NH}}(\boldsymbol{k})}{k_0^2+(1-\beta)^2v_{\mathrm{F}}^2|\boldsymbol{k}|^2}\\ &\quad\times\frac{k_0^2+(1+\beta^2)v_{\mathrm{F}}^2|\boldsymbol{k}|^2-2\beta v_{\mathrm{F}}^2H_1(\boldsymbol{k})H_2(\boldsymbol{k})}{\sqrt{\dfrac{(p_0-k_0)^2}{c^2}+(\boldsymbol{p}-\boldsymbol{k})^2}}\gamma_\mu.\end{aligned}\tag{A1}$$

Using dimensional regularization in $d=3-\varepsilon$ dimensions and performing the momentum integration, we obtain

$$\begin{aligned}\Sigma_{1\,\mathrm{loop}}(p) = \frac{3e^2}{16\pi^2\varepsilon c}\left[\frac{1}{\varepsilon}+O(\varepsilon^0)\right]\int_0^1\mathrm{d}x\int_0^{1-x}\mathrm{d}y\frac{\sqrt{1-x-y}}{f(x,y)}\Bigg\{&\left[1-2(1+\beta^2)\frac{v_{\mathrm{F}}^2}{c^2}+\frac{2(1+\beta^2)\frac{v_{\mathrm{F}}^2}{c^2}-4(1+\beta^4)\frac{v_{\mathrm{F}}^4}{c^4}}{3f(x,y)}\right](\mathrm{i}p_0)\\ &-2\beta\frac{v_{\mathrm{F}}^2}{c^2}\left[1+\frac{1+2(1+\beta^2)\frac{v_{\mathrm{F}}^2}{c^2}}{3f(x,y)}\right](\Gamma_{11}+\Gamma_{22})(\mathrm{i}p_0)+\frac{8\beta^2\frac{v_{\mathrm{F}}^4}{c^4}}{3f(x,y)}\Gamma_{33}(\mathrm{i}p_0)\\ &-\left[\frac{1-4\beta^2\frac{v_{\mathrm{F}}^2}{c^2}}{3f(x,y)}+\frac{4(1-\beta^2)\frac{v_{\mathrm{F}}^2}{c^2}}{3f^2(x,y)}\right]v_{\mathrm{H}}(1+\alpha M)(\Gamma_{10}p_1+\Gamma_{20}p_2)-\left[\frac{1-4\frac{v_{\mathrm{F}}^2}{c^2}}{3f(x,y)}-\frac{4(1-\beta^2)\frac{v_{\mathrm{F}}^2}{c^2}}{3f^2(x,y)}\right]\beta\frac{v_{\mathrm{F}}^2}{c^2}(\Gamma_{01}p_1+\Gamma_{02}p_2)\Bigg\}\end{aligned}\tag{A2}$$

where the auxiliary function $f(x,y)$ is defined as

$$f(x,y)=1-x\left[1-(1+\beta)^2\frac{v_{\mathrm{F}}^2}{c^2}\right]-y\left[1-(1-\beta)^2\frac{v_{\mathrm{F}}^2}{c^2}\right].\tag{A3}$$

The counterterm of the fermionic self-energy diagram takes the form

$$\begin{aligned}\Sigma_{\mathrm{ct}}(p) = &-(Z_\psi-1)\mathrm{i}p_0-(Z_\psi Z_{v_{\mathrm{H}}}-1)v_{\mathrm{H}}\sum_{j=1}^{d}\Gamma_{j0}p_j-(Z_\psi Z_\alpha Z_{v_{\mathrm{H}}}-1)\alpha v_{\mathrm{H}}M\sum_{j=1}^{d}\Gamma_{j0}p_j\\ &-(Z_\psi Z_\beta Z_{v_{\mathrm{H}}}-1)\beta v_{\mathrm{H}}\sum_{j=1}^{d}\Gamma_{0j}p_j-(Z_\psi Z_\alpha Z_\beta Z_{v_{\mathrm{H}}}-1)\alpha\beta v_{\mathrm{H}}M\sum_{j=1}^{d}\Gamma_{0j}p_j.\end{aligned}\tag{A4}$$

By requiring that the divergences in the one-loop self-energy are canceled by these counterterms, we obtain the following renormalization constants:

$$\begin{aligned}&Z_\alpha=1,\\ &Z_\psi=1+\frac{3e^2}{16\pi^2\varepsilon c}\frac{1}{\varepsilon}\int_0^1\mathrm{d}x\int_0^{1-x}\mathrm{d}y\frac{\sqrt{1-x-y}}{f(x,y)}\left[1-2(1+\beta^2)\frac{v_{\mathrm{F}}^2}{c^2}+\frac{2(1+\beta^2)\frac{v_{\mathrm{F}}^2}{c^2}-4(1+\beta^4)\frac{v_{\mathrm{F}}^4}{c^4}}{3f(x,y)}\right],\end{aligned}$$

$$
\begin{aligned}
Z_\psi Z_{v_{\rm H}} &= 1-\frac{3e^2}{16\pi^2\varepsilon c}\frac{1}{\varepsilon}\int_0^1 {\rm d}x\int_0^{1-x}{\rm d}y\frac{\sqrt{1-x-y}}{f(x,y)}\left[\frac{1-4\beta^2\frac{v_{\rm F}^2}{c^2}}{3f(x,y)}+\frac{4(1-\beta^2)\frac{v_{\rm F}^2}{c^2}}{3f^2(x,y)}\right],\\
Z_\psi Z_{v_{\rm H}} Z_\beta &= 1-\frac{3e^2}{16\pi^2\varepsilon c}\frac{1}{\varepsilon}\int_0^1 {\rm d}x\int_0^{1-x}{\rm d}y\frac{\sqrt{1-x-y}}{f(x,y)}\left[\frac{1-4\frac{v_{\rm F}^2}{c^2}}{3f(x,y)}-\frac{4(1-\beta^2)\frac{v_{\rm F}^2}{c^2}}{3f^2(x,y)}\right],\\
Z_{v_{\rm H}} &= 1-\frac{3e^2}{16\pi^2\varepsilon c}\frac{1}{\varepsilon}\int_0^1 {\rm d}x\int_0^{1-x}{\rm d}y\frac{\sqrt{1-x-y}}{f(x,y)}\\
&\quad\times\left[1-2(1+\beta^2)\frac{v_{\rm F}^2}{c^2},+\frac{1+2(1-\beta^2)\frac{v_{\rm F}^2}{c^2}-4(1+\beta^4)\frac{v_{\rm F}^4}{c^4}}{3f(x,y)}+\frac{4(1-\beta^2)\frac{v_{\rm F}^2}{c^2}}{3f^2(x,y)}\right],\\
Z_\beta &= 1+\frac{3e^2}{16\pi^2\varepsilon c}\frac{1}{\varepsilon}\int_0^1 {\rm d}x\int_0^{1-x}{\rm d}y\frac{\sqrt{1-x-y}}{f(x,y)}\left[\frac{4(1-\beta^2)\frac{v_{\rm F}^2}{c^2}}{3f(x,y)}+\frac{8(1-\beta^2)\frac{v_{\rm F}^2}{c^2}}{3f^2(x,y)}\right].
\end{aligned}
$$

Since the bare parameters are independent of the renormalization scale μ, we can derive the renormalization group equations

$$
\begin{aligned}
\mu\frac{{\rm d}v_{\rm H}}{{\rm d}\mu} &= -\frac{3e^2}{16\pi^2\varepsilon}\frac{v_{\rm H}}{c}\left\{\left[1-2(1+\beta^2)\frac{v_{\rm F}^2}{c^2}\right]F_1(v_{\rm F},\beta)+\left[1+2(1-\beta^2)\frac{v_{\rm F}^2}{c^2}-4(1+\beta^4)\frac{v_{\rm F}^4}{c^4}\right]F_2(v_{\rm F},\beta)\right.\\
&\quad\left.+4(1-\beta^2)\frac{v_{\rm F}^2}{c^2}F_3(v_{\rm F},\beta)\right\},\\
\mu\frac{{\rm d}\beta}{{\rm d}\mu} &= \frac{3e^2}{16\pi^2\varepsilon}\frac{\beta}{c}4(1-\beta^2)\frac{v_{\rm F}^2}{c^2}[F_2(v_{\rm F},\beta)+2F_3(v_{\rm F},\beta)],
\end{aligned}
\tag{A5}
$$

where the auxiliary functions are defined as

$$
F_1(v_{\rm F},\beta)=\int_0^1{\rm d}x\int_0^{1-x}{\rm d}y\frac{\sqrt{1-x-y}}{f(x,y)},\quad F_2(v_{\rm F},\beta)=\int_0^1{\rm d}x\int_0^{1-x}{\rm d}y\frac{\sqrt{1-x-y}}{3f^2(x,y)},\ F_3(v_{\rm F},\beta)\quad=\int_0^1{\rm d}x\int_0^{1-x}{\rm d}y\frac{\sqrt{1-x-y}}{3f^3(x,y)}.
$$

These RG equations describe the scaling behavior of the system parameters and determine their evolution under changes in the energy scale, as discussed in detail in the main text.

A2. Vertex correction

The vertex correction to the lowest order in perturbation theory is given by

$$
\begin{aligned}
\boldsymbol{V}_0 &= e^3\int\frac{{\rm d}^3k}{(2\pi)^3}\gamma_\rho S(k)\gamma_0 S(k)\gamma_\nu\tilde{D}_{\nu\rho}(k)\\
&=\frac{{\rm i}e^3}{2\varepsilon}\int\frac{{\rm d}^3k}{(2\pi)^3}\frac{\gamma_\rho[{\rm i}k_0+H_{\rm BF,NH}]}{[k_0^2+(1+\beta)^2v_{\rm F}^2|\boldsymbol{k}|^2]^2}\frac{[k_0^2+(1+\beta^2)v_{\rm F}^2|\boldsymbol{k}|^2-2\beta v_{\rm F}^2H_1H_2][{\rm i}k_0+H_{\rm BF,NH}]}{[k_0^2+(1-\beta)^2v_{\rm F}^2|\boldsymbol{k}|^2]^2}\frac{[k_0^2+(1+\beta^2)v_{\rm F}^2|\boldsymbol{k}|^2-2\beta v_{\rm F}^2H_1H_2]\gamma_\rho}{\sqrt{\frac{k_0^2}{c^2}+k_1^2+k_2^2}}\\
&=\frac{105{\rm i}e^3}{64\pi^2\varepsilon c}\left[\frac{1}{\varepsilon}+O(\varepsilon^0)\right]\int_0^1{\rm d}x\int_0^{1-x}{\rm d}y\frac{xy}{\sqrt{1-x-y}}\frac{1}{f(x,y)}\left\{\left[\frac{1}{7}+\frac{2(1+\beta^2)\frac{v_{\rm F}^2}{c^2}}{35f}-\frac{8(1-10\beta^2+\beta^4)\frac{v_{\rm F}^4}{c^4}}{105f^2}\right.\right.\\
&\quad\left.-\frac{16(1-\beta^2)(1-\beta^4)\frac{v_{\rm F}^6}{c^6}}{35f^3}\right]\left[1-2(1+\beta^2)\frac{v_{\rm F}^2}{c^2}-2\beta\frac{v_{\rm F}^2}{c^2}(\Gamma_{11}+\Gamma_{22})\right]\\
&\quad\left.+\left[\frac{6\beta\frac{v_{\rm F}^2}{c^2}}{35f}+\frac{16\beta(1+\beta^2)\frac{v_{\rm F}^4}{c^4}}{105f^2}-\frac{16\beta(1-\beta^2)^2\frac{v_{\rm F}^6}{c^6}}{35f^3}\right]\left[4\beta\frac{v_{\rm F}^2}{c^2}(1+\Gamma_{33})-(\Gamma_{11}+\Gamma_{22})\right]\right\}.
\end{aligned}
$$

Using the minimal subtraction renormalization condition

$$
Z_\Psi Z_e Z_A^{1/2}{\rm i}e+\boldsymbol{V}_0={\rm i}e,
\tag{A6}
$$

we obtain

$$
\begin{aligned}
Z_\Psi Z_e Z_A^{1/2} &= 1-\frac{15e^2}{64\pi^2\varepsilon c}\frac{1}{\varepsilon}\int_0^1{\rm d}x\int_0^{1-x}{\rm d}y\frac{xy}{f(x,y)(1-x-y)^{\frac{1}{2}}}\left\{\left[1-2(1+\beta^2)\frac{v_{\rm F}^2}{c^2}\right]\right.\\
&\quad\left.\times\left[1+\frac{2(1+\beta^2)\frac{v_{\rm F}^2}{c^2}}{5f}-\frac{8(1-10\beta^2+\beta^4)\frac{v_{\rm F}^4}{c^4}}{15f^2}-\frac{16(1-\beta^2)(1-\beta^4)\frac{v_{\rm F}^6}{c^6}}{5f^3}\right]\right.
\end{aligned}
$$

$$+4\beta\frac{v_{\rm F}^2}{c^2}\left[\frac{6\beta\frac{v_{\rm F}^2}{c^2}}{5f}+\frac{16\beta(1+\beta^2)\frac{v_{\rm F}^4}{c^4}}{15f^2}-\frac{16\beta(1-\beta^2)^2\frac{v_{\rm F}^6}{c^6}}{5f^3}\right]\Bigg\}.$$

Similarly, for the spatial components of the vertex ($j=1,2$),

$$\begin{aligned}
\boldsymbol{V}_j &= e^3\int\frac{{\rm d}^3k}{(2\pi)^3}\gamma_\rho S(k)\gamma_1 S(k)\gamma_\nu\tilde{D}_{\nu\rho}(k)\\
&= \frac{e^3}{2\varepsilon}\int\frac{{\rm d}^3k}{(2\pi)^3}\frac{\gamma_\rho[{\rm i}k_0+H_{\rm BF,NH}]}{[k_0^2+(1+\beta)^2v_{\rm F}^2|\boldsymbol{k}|^2]^2}\frac{[k_0^2+(1+\beta^2)v_{\rm F}^2|\boldsymbol{k}|^2-2\beta v_{\rm F}^2H_1H_2]\gamma_1}{[k_0^2+(1-\beta)^2v_{\rm F}^2|\boldsymbol{k}|^2]^2}\\
&\quad\times\frac{[{\rm i}k_0+H_{\rm BF,NH}][k_0^2+(1+\beta^2)v_{\rm F}^2|\boldsymbol{k}|^2-2\beta v_{\rm F}^2H_1H_2]\gamma_\rho}{\sqrt{\frac{k_0^2}{c^2}+k_1^2+k_2^2}}\\
&= \frac{105e^3}{64\pi^2\varepsilon c}\left[\frac{1}{\varepsilon}+O(\varepsilon^0)\right]\int_0^1{\rm d}x\int_0^{1-x}{\rm d}y\frac{xy}{\sqrt{1-x-y}}\frac{1}{f(x,y)}\\
&\quad\times\Bigg\{\left[\frac{1-4\beta^2\frac{v_{\rm F}^2}{c^2}}{7}+\frac{4(1-\beta^2)\frac{v_{\rm F}^2}{c^2}}{35f}+\frac{16(1-\beta^4)\frac{v_{\rm F}^4}{c^4}}{105f^2}-\frac{8(1-\beta^2)^2\frac{v_{\rm F}^4}{c^4}(1-4\beta^2\frac{v_{\rm F}^2}{c^2})}{105f^2}\right]\\
&\quad\times\frac{v_{\rm H}}{c}(1+\alpha M)\Gamma_{j0}+\left[\frac{1-4\frac{v_{\rm F}^2}{c^2}}{7}-\frac{4(1-\beta^2)\frac{v_{\rm F}^2}{c^2}}{35f}-\frac{16(1-\beta^4)\frac{v_{\rm F}^4}{c^4}}{105f^2}-\frac{8(1-\beta^2)^2\frac{v_{\rm F}^4}{c^4}(1-4\frac{v_{\rm F}^2}{c^2})}{105f^2}\right]\\
&\quad\times\beta\frac{v_{\rm H}}{c}(1+\alpha M)\Gamma_{0j}\Bigg\},\quad(j=1,2).
\end{aligned}$$

The minimal subtraction renormalization condition gives

$$e\frac{v_{\rm H}}{c}(1+Z_\alpha\alpha M)Z_\Psi Z_e Z_A^{1/2}Z_{v_{\rm H}}\left(\Gamma_{j0}+Z_\beta\beta\Gamma_{0j}\right)+\boldsymbol{V}_j=e\frac{v_{\rm H}}{c}(1+\alpha M)\left(\Gamma_{j0}+\beta\Gamma_{0j}\right).\tag{A7}$$

These vertex corrections, together with the self-energy calculated earlier, satisfy the Ward identity in quantum electrodynamics of birefringent Dirac fermions. This can be expressed more compactly as

$$\frac{\partial\Sigma_{1\,\rm loop}(p)}{\partial p_0}=-\frac{1}{e}\boldsymbol{V}_0,\tag{A8}$$

$$\frac{\partial\Sigma_{1,\,\rm loop}(p)}{\partial p_j}=-\frac{c}{e}\boldsymbol{V}_j,\quad(j=1,2).\tag{A9}$$

We have numerically verified these Ward identities by showing that the relevant integral combinations vanish for all physical values of $v_{\rm F}$ and β, except near the singular points $v_{\rm F}=0$ and $\beta=1$ where the integrals diverge.

A3. Ward identity

To verify the Ward identities in our non-Hermitian birefringent quantum electrodynamics system, we perform detailed numerical calculations of the relevant integral combinations. The Ward identities relating the vertex corrections to the self-energy derivatives can be expressed as

$$\frac{\partial\Sigma_{1\,\rm loop}(p)}{\partial p_0}=-\frac{1}{e}\boldsymbol{V}_0,\tag{A10}$$

$$\frac{\partial\Sigma_{1\,\rm loop}(p)}{\partial p_j}=-\frac{c}{e}\boldsymbol{V}_j,\quad(j=1,2).\tag{A11}$$

Based on the previously calculated Fermi self-energy and vertex correction, compute the difference between the left-hand side and the right-hand side of Eq. (A10) for the time component (setting $c=1$):

$$\begin{aligned}
&\int_0^1{\rm d}x\int_0^{1-x}{\rm d}y\frac{(1-x-y)^{\frac{1}{2}}}{f(x,y)}\left[\frac{1-4\beta^2v_{\rm F}^2}{3f(x,y)}+\frac{4(1-\beta^2)v_{\rm F}^2}{3f^2(x,y)}\right]\\
&-\int_0^1{\rm d}x\int_0^{1-x}{\rm d}y\frac{xy}{f(x,y)(1-x-y)^{1/2}}\\
&\times\left[\frac{5}{4}-5\beta^2v_{\rm F}^2+\frac{(1-\beta^2)v_{\rm F}^2}{f}+\frac{4(1-\beta^4)v_{\rm F}^4}{3f^2}\right.\\
&\left.-\frac{2(1-\beta^2)^2v_{\rm F}^4(1-4\beta^2v_{\rm F}^2)}{3f^2}\right].
\end{aligned}\tag{A12}$$

Similarly, for the spatial components, calculate the difference between the left-hand side and the right-hand side of Eq. (A11) (setting $c=1$):

$$\begin{aligned}
&\int_0^1{\rm d}x\int_0^{1-x}{\rm d}y\frac{\sqrt{1-x-y}}{f(x,y)}\left[\frac{1-4v_{\rm F}^2}{3f(x,y)}-\frac{4(1-\beta^2)v_{\rm F}^2}{3f^2(x,y)}\right]\\
&-\int_0^1{\rm d}x\int_0^{1-x}{\rm d}y\frac{xy}{f(x,y)(1-x-y)^{1/2}}\\
&\times\left[\frac{5}{4}-5v_{\rm F}^2-\frac{(1-\beta^2)v_{\rm F}^2}{f}-\frac{4(1-\beta^4)v_{\rm F}^4}{3f^2}\right.\\
&\left.-\frac{2(1-\beta^2)^2v_{\rm F}^4(1-4v_{\rm F}^2)}{3f^2}\right].
\end{aligned}$$

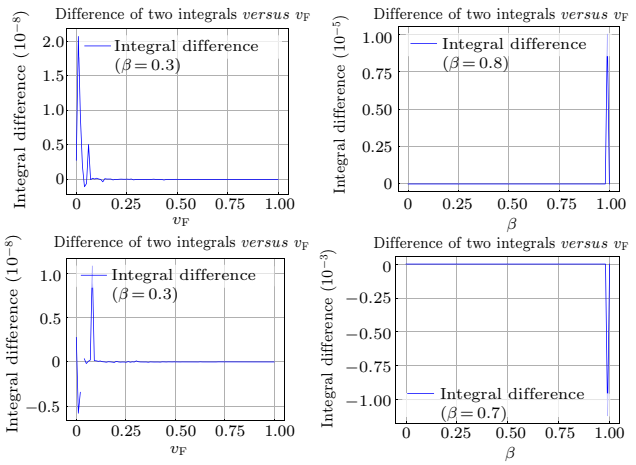


Fig. A1. Numerical verification of Ward identities. (a) Temporal Ward identity as a function of v_F with fixed $\beta = 0.3$. (b) Temporal Ward identity *versus* β at fixed $v_F = 0.8$. (c) Spatial Ward identity as a function of v_F with $\beta = 0.3$. (d) Spatial Ward identity *versus* β at $v_F = 0.7$. The vanishing integral differences confirm the validity of both temporal and spatial Ward identities throughout the physical parameter space, except at the singular points $v_F = 0$ and $\beta = 1$ where the integrals diverge.

Our numerical analysis demonstrates that these integral combinations vanish across a wide range of physical parameters. Figures A1(a)–A1(d) show the evaluation of the temporal Ward identity as functions of v_F and β respectively. The results confirm that the identity holds except near singular points $v_F = 0$ and $\beta = 1$, where the integrals exhibit divergent behavior due to the breakdown of our perturbative approach.

The numerical verification of these Ward identities provides strong evidence for the gauge invariance of our theory, even in the presence of both non-Hermiticity and birefringence. This remarkable result suggests that the fundamental relationship between vertex corrections and self-energy, which is crucial for maintaining gauge invariance in conventional quantum electrodynamics, persists in our non-Hermitian birefringent extension. The breakdown of these identities at $v_F = 0$ and $\beta = 1$ marks the boundaries of validity for our perturbative approach and coincides with physical singularities in the system.

Acknowledgements

Project supported by the National Key Research and Development Program of China (Grants Nos. 2021YFA1400900, 2021YFA0718300, and 2021YFA1400243), the National Natural Science Foundation of China (Grant Nos. 61835013, 12174461, and 12234012), and the Fund from the Space Application System of China Manned Space Program.

References

[1] Kawabata K, Shiozaki K, Ueda M and Sato M 2019 *Phys. Rev. X* **9** 041015
[2] Hurst H M and Flebus B 2022 *J. Appl. Phys.* **132** 220902
[3] Cao H and Wiersig J 2015 *Rev. Mod. Phys.* **87** 61
[4] Roccati F and Palma G M, Ciccarello F and Bagarello F 2022 *Open Systems and Information Dynamics* **29** 2250004
[5] Rahul S and Sarkar S 2022 *Sci. Rep.* **12** 6993
[6] Zhao W L and Liu J 2024 *Phys. Rev. A* **109** 052215
[7] Hsieh C T and Chang P Y 2023 *SciPost Physics Core* **6** 062
[8] Li C, Wu Y and Liu W M 2024 *Phys. Rev. B* **109** 214306
[9] Wang H Y and Liu W M 2022 *Phys. Rev. A* **106** 052216
[10] Wang H Y, Yang Z B and Liu W M 2024 *Quantum Science and Technology* **9** 025019
[11] Wang H and Liu W 2023 *Physica A* **619** 128733
[12] Martinez Alvarez V, Barrios Vargas J, Berdakin M and Foa Torres L 2018 *Eur. Phys. J. Special Topics* **227** 1295
[13] Zhang K, Yang Z and Fang C 2022 *Phys. Rev. A* **106** 052216
[14] Della Valle F, Ejlli A, Gastaldi U, Messineo G, Milotti E, Pengo R, Ruoso G and Zavattini G 2016 *Eur. Phys. J. C* **76** 1
[15] Chen C, Wang S S, Liu L, Yu Z M, Sheng X L, Chen Z and Yang S A 2017 *Phys. Rev. Mater.* **1** 044201
[16] Cerjan A, Huang S, Wang M, Chen K P, Chong Y and Rechtsman M C 2019 *Nat. Photon.* **13** 623
[17] Juričić V and Roy B 2024 *Commun. Phys.* **7** 169
[18] Roy B, Smith P M and Kennett M P 2012 *Phys. Rev. B* **85** 235119
[19] Peng Y, Jie J, Yu D and Wang Y 2022 *Phys. Rev. B* **106** L161402
[20] Li C A, Trauzettel B, Neupert T and Zhang S B 2023 *Phys. Rev. Lett.* **131** 116601
[21] Lu M, Zhang X X and Franz M 2021 *Phys. Rev. Lett.* **127** 256402
[22] Jung C, Müller M and Rotter I 1999 *Phys. Rev. E* **60** 114
[23] Berry M and Dennis M 2003 *Proc. Roy. Soc. London. Ser. A: Math. Phys. Eng. Sci.* **459** 1261
[24] Król M, Septembre I, Oliwa P, Kędziora M, Łempicka-Mirek K, Muszyński M, Mazur R, Morawiak P, Piecek W, Kula P, *et al.* 2022 *Nat. Commun.* **13** 5340
[25] Gupta S K, Zou Y, Zhu X Y, Lu M H, Zhang L J, Liu X P and Chen Y F 2020 *Adv. Mater.* **32** 1903639
[26] Murshed S A and Roy B 2024 *Journal of High Energy Physics* **2024** 1
[27] Metzner W, Salmhofer M, Honerkamp C, Meden V and Schönhammer K 2012 *Rev. Mod. Phys.* **84** 299
[28] Benfatto G and Gallavotti G 1990 *Phys. Rev. B* **42** 9967
[29] Gentile G and Mastropietro V 2001 *Phys. Rep.* **352** 273
[30] Jones-Smith K and Mathur H 2014 *Phys. Rev. D* **89** 125014
[31] Lima F, Monteiro L and Almeida C 2023 *Physica E* **150** 115682
[32] Gomes Y 2024 *Eur. Phys. J. C* **84** 1
[33] Jebraeilli A and Geller M R 2025 *Phys. Rev. A* **111** 032211
[34] Romito A 2023 *Nat. Phys.* **19** 1234
[35] Long Y, Xue H and Zhang B 2022 *Phys. Rev. B* **105** L100102
[36] Zhang B, Li Q, Zhang X and Lee C H 2022 *Chin. Phys. B* **31** 070308
[37] Liu T, He J J, Yang Z and Nori F 2021 *Phys. Rev. Lett.* **127** 196801
[38] Leibbrandt G 1975 *Rev. Mod. Phys.* **47** 849
[39] Xu H Y, Wang G L, Huang L and Lai Y C 2018 *Phys. Rev. Lett.* **120** 124101
[40] Roy B and Juričić V 2020 *Phys. Rev. Res.* **2** 012047
[41] Onuma T and Otani Y 2014 *Opt. Commun.* **315** 69
[42] Otani Y, Shimada T, Yoshizawa T and Umeda N 1994 *Optical Engineering* **33** 1604
[43] Murshed S A and Roy B 2025 *SciPost Physics* **18** 073
[44] Cerjan A and Fan S 2017 *Phys. Rev. Lett.* **118** 253902
[45] Golubtsova A, Nikolaev A and Podoinitsyn M 2024 *Phys. Rev. D* **110** 066011